Evidence for a Grotthuss-Like Mechanism in the Formation of the Rhamnose Alkoxy Radical Based on Periodic DFT Calculations

Authors: Pauwels, Ewald, Declerck, Reinout, Speybroeck, Veronique Van, and Waroquier, Michel

Source: Radiation Research, 169(1) : 8-18

Published By: Radiation Research Society

URL: https://doi.org/10.1667/RR1039.1

RADIATION RESEARCH **169**, 8–18 (2008)
0033-7587/08 $15.00

Evidence for a Grotthuss-Like Mechanism in the Formation of the Rhamnose Alkoxy Radical Based on Periodic DFT Calculations

Ewald Pauwels,[1] Reinout Declerck, Veronique Van Speybroeck and Michel Waroquier

Center for Molecular Modeling, Ghent University, Proeftuinstraat 86, B-9000 Gent, Belgium

Pauwels, E., Declerck, R., Van Speybroeck, V. and Waroquier, M. Evidence for a Grotthuss-Like Mechanism in the Formation of the Rhamnose Alkoxy Radical Based on Periodic DFT Calculations. *Radiat. Res.* 169, 8–18 (2008).

Molecular modeling adopting a periodic approach based on density functional theory (DFT) indicates that a Grotthuss-like mechanism is active in the formation of the radiation-induced alkoxy radical in α-L-rhamnose. Starting from an oxidized crystal structure, a hydroxyl proton is transferred along an infinite hydrogen bond chain pervading the entire crystal. The result of this proton shuttling mechanism is a stable radical species dubbed RHop. Only after several reorientations of crystal waters and hydroxyl groups, the more stable radical form RO4 is obtained, which differs in structure from the former by the absence of only one hydrogen bond. Calculations of the energetics associated with the mechanism as well as simulated spectroscopic properties reveal that different variants of the rhamnose alkoxy radical can be observed depending on the temperature of irradiation and consecutive EPR measurement. Cluster calculations on both radical variants provide hyperfine coupling and *g* tensors that are in good agreement with two independent experimental measurements at different temperatures.

INTRODUCTION

The radiation chemistry of solid-state sugars has attracted considerable attention, because these highly structured systems can function as model systems to study radiation damage in biomolecules from a general perspective. The involvement of deoxyribose sugar radicals in radiation-induced single-strand breaks of DNA has added to the interest in this subject (*1, 2*), which only recently led to the unambiguous identification and characterization of such radicals in irradiated nucleotides (*3, 4*). However, the exact processes that lead to the formation of radical end products are not known. In an attempt to clarify the initial radiation-induced events, several electron paramagnetic resonance (EPR) studies have been performed on single-crystal sugars at very low temperatures [e.g. ref. (*5*)]. The lack of thermal energy limits the conversion of primary radiation products in secondary reactions, and this allows thorough EPR characterization of the former. One of the archetypal systems in this respect is α-rhamnose, since both oxidation and reduction products have been observed in this sugar. Reduction results in the ''trapping'' of low-energy electrons at intermolecular sites within the crystal matrix, stabilized through the cumulative effect of dipolar molecules or functional groups in the vicinity (*6–8*). Ionization-induced oxidation of rhamnose leads to the formation of an oxygen-centered alkoxy radical (*9, 10*). Several of the secondary radiation-induced radicals have also been characterized in rhamnose and are generally considered to be decay products of the previous primary species under the influence of temperature or light (*7, 8, 11*).

In an earlier theoretical study, we investigated the primary alkoxy and several secondary rhamnose radicals using density functional theory (DFT) calculations (*12*). Adopting a cluster approach, the radical model under scrutiny was surrounded by several intact rhamnose molecules in accordance with crystallography data, and EPR properties were calculated on the optimal conformation of the model. Comparison of calculated *g* and hyperfine tensors and experimental data resulted in the independent identification and corroboration of the radical structures that were proposed in the various EPR experiments. It also led to the assignment of a completely new radical structure to one of the observed species. For the alkoxy radical, however, an unusual discrepancy was encountered. Calculated EPR properties were found to be in accordance with only one of the two EPR measurements on this radical that are available in literature.

In 1980, Samskog and Lund performed a Q-band ESR measurement at 77 K of the alkoxy radical and determined its *g* tensor along with two hyperfine coupling constants (*9*). Five years later, Budzinski and Box used a combination of both ESR and ENDOR to thoroughly characterize this species at 4.2 K (*10*). They succeeded in deriving the *g* tensor and seven hyperfine tensors. An overview of the measured data is given in Table 1, although several likely errors in the data from the original manuscript were corrected (a detailed discussion is given as Supplementary Information). We will refer to the results of these experiments with the notations Alk_{BB} and Alk_{SL}, respectively. From the table, it can easily be seen that the two data sets are very

[1] Address for correspondence: Center for Molecular Modeling, Ghent University, Proeftuinstraat 86, B-9000 Gent, Belgium; e-mail: ewald.pauwels@UGent.be.

TABLE 1
Summary of EPR Measurements and Previous DFT Calculations on Rhamnose Alkoxy Radical

Signal	A_{iso}/g_{iso}	A_{aniso}/g_{aniso}	Direction cosines vs ⟨a*bc⟩		
Alk_{SL} (77 K)[a]					
SL-1	112.1				
SL-2	39.2				
SL-g	2.0184	2.0032	−0.020	−0.982	0.189
		2.0064	−0.698	0.149	0.700
		2.0456	−0.716	−0.118	−0.688
Alk_{BB} (4.2 K)[b]					
BB-1	−3.0	−7.7	0.127	0.003	0.991
		−7.3	0.990	0.056	−0.127
		15.1	−0.056	0.998	0.003
BB-2	5.2	−12.7	−0.136	0.176	0.975
		−0.2	0.787	0.616	−0.001
		12.9	−0.601	0.767	−0.222
BB-3 (xc)	0.1	−5.9	−0.023	0.221	0.974
		−4.9	0.364	0.909	−0.197
		10.8	0.930	−0.351	0.102
BB-4 (xc)	5.2	−7.8	0.259	−0.079	0.962
		−0.1	0.744	0.651	−0.146
		7.9	−0.615	0.754	0.227
BB-5	67.2	−4.0	0.743	−0.481	−0.464
		−0.2	0.409	−0.220	0.884
		4.3	0.528	0.848	−0.033
BB-6	53.9	−7.7	0.219	0.687	0.691
		−2.0	−0.377	−0.594	0.710
		9.7	0.899	−0.417	0.129
BB-7	3.9	−1.9	0.696	−0.607	0.381
		−0.7	0.584	0.789	0.189
		2.6	−0.416	0.091	0.904
BB-g	2.0096	2.0018	−0.339	−0.691	0.637
		2.0068	−0.554	0.694	0.458
		2.0202	−0.759	−0.198	−0.619
RO4 (cluster DFT)[c]					
H2	40.5				
H4	100.4				
g tensor	2.0189	2.0022	−0.251	−0.885	0.392
		2.0090	−0.690	0.448	0.569
		2.0456	−0.679	−0.128	−0.723

Note. Hyperfine couplings are in MHz.
[a] Reference (*9*).
[b] Reference (*10*).
[c] Reference (*12*).

dissimilar, as already noted by Sagstuen *et al.* (*11*). The Alk_{SL} species is characterized by two isotropic splittings (112 and 39 MHz) that cannot be matched with the two largest couplings (67 and 54 MHz) in Alk_{BB}. Furthermore, the maximum anisotropic component of the *g* tensor differs between the two sets: 2.0456 in Alk_{SL} and 2.0202 in Alk_{BB}. In particular, the latter difference is surprising since the corresponding eigenvectors deviate by only a few degrees. Despite these clear distinctions, an identical structure was assigned in both studies, represented in Fig. 1.

Recent theoretical calculations (*12*) on this suggested structure were found to be in complete accordance with the EPR data of Samskog and Lund: hyperfine couplings of 40 and 100 MHz, and a maximum *g*-tensor component of 2.0456 (see calculated **RO4** data in Table 1). Given the temperature difference between the two EPR measurements, it was assumed that Alk_{BB} represents a precursor to the Alk_{SL} structure and differs from the latter mainly because of the closeness of the dissociated H_{O4} hydroxyl proton in the former (see Fig. 1 for atom numbering scheme). In the Alk_{BB} measurements, a hyperfine coupling tensor was determined for this proton, indicating that it is generally situated in the direction of the original O_4–H_{O4} bond.

In the current work, we present the results of new calculations based on a periodic DFT approach in which the origin of this discrepancy is investigated. Starting from the primary radical cation species, generated directly by radiation, proton transfer reactions are considered within the

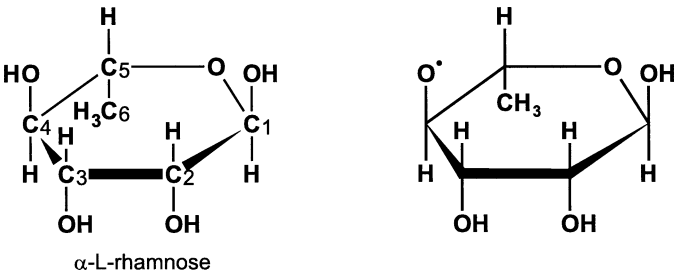

FIG. 1. Atom numbering in α-L-rhamnose and structure of the alkoxy radical. Oxygens and hydrogens are numbered according to the carbon to which they are bound.

solid state. A mechanism is found that likely connects the Alk_{BB} precursor at very low temperature with the Alk_{SL} radical at 77 K. Energetic considerations are corroborated by theoretical EPR calculations on the suggested species, which are in agreement with the experimental EPR data for both the Alk_{SL} and Alk_{BB} species.

COMPUTATIONAL DETAILS

A simulation study of proton transfer reactions between the rhamnose radical and its molecular environment is meaningful only if as little constraint as possible is imposed on the latter. The surrounding molecule(s) in the solid must be able to accommodate the proton that is transferred through atomic relaxation. This requirement seriously limits the use of cluster models in this respect. As adopted in the previous paper (*12*), the smallest rhamnose cluster model that is physically sound already consists of the radical, seven rhamnose molecules, and eight water molecules—those molecules that are involved in hydrogen bonds with the central paramagnetic species. However, only the atoms of the radical were allowed to relax in this model. To enable relaxation of the closest hydrogen-bonded species, it is necessary to expand the cluster with an additional layer: Every hydrogen bond partner of the radical has to be surrounded in a similar fashion by its hydrogen bond partners, all in accordance with the rhamnose crystal symmetry. The resulting supercluster (containing more than 500 atoms) is far too large to be computationally feasible at a reasonable level of theory. The outermost shell of rhamnose/water molecules still has to be constrained because it is at the boundary between the cluster and the vacuum. A more effective and natural way to simulate the radical and its solid-state environment is to perform periodic calculations, thereby exploiting the translational symmetry of the crystalline state. Hence the lattice environment is automatically and fully incorporated, and no constraints are needed on the hydrogen-bonded species.

The unit cell of rhamnose is monoclinic (space group symmetry $P2_1$) and contains two rhamnose and two water molecules. Its cell parameters are $a = 7.901$ Å, $b = 7.922$ Å, $c = 6.670$ Å and $\beta = 95.52°$ (*13*). To ensure that the radical is well separated from its periodic images, the original unit cell was doubled in all directions. The resulting ⟨2a2b2c⟩ supercell contains 416 atoms. All calculations were performed using the CPMD software package (*14*). The BP86 gradient-corrected density functional (*15, 16*) was used, together with a plane wave basis set (cutoff 25 Ry) and ultrasoft pseudopotentials of the Vanderbilt type to describe the electron-ion interaction (*17*). To corroborate the results obtained with a ⟨2a2b2c⟩ supercell, several simulations were also performed with the ⟨a2bc⟩ and ⟨a3bc⟩ supercells, obtained by respectively doubling and tripling the original unit cell in the *b* direction.

Subsequently, EPR properties were calculated (*18*) on the structures obtained from the periodic ⟨2a2b2c⟩ optimizations. As ascertained in other studies, the environment of a radical has a significant impact on these properties. Hence it is imperative to include this environment also in the EPR calculation, either using a periodic scheme (*19*) or by adopting a cluster approach (*12, 20, 21*). To allow direct comparison with the EPR results in the earlier study of rhamnose (*12*), the latter approach was chosen. After optimization, a cluster was cut out of the periodic system to contain the radical and all the molecules that are hydrogen bound to it (seven rhamnose and eight water molecules). This is the same model space that was used in the previous study, but it was adopted only for the EPR calculation. The benefit of such a hybrid periodic/cluster scheme is that the EPR properties of the radical can be determined consistently with cluster methods, while the structural information obtained from geometry optimization in a periodic approach can still be maintained.

Hyperfine tensors were calculated using the Gaussian03 software suite (*22*), using the B3LYP functional (*23*) and a 6-311G** basis set (*24, 25*) for all atoms within the cluster. However, this level of theory is too expensive from a computational point of view for the calculation of *g* tensors. This difficulty can be overcome either by reducing the model system (taking up fewer molecules in the calculation) or by reducing the level of theory for (part of) the model system. The first approximation was adopted in the previous study (*12*), and only the rhamnose radical itself was considered in the *g*-tensor calculation. Since this is an approach that can essentially provide only gas-phase properties, the second option was preferred in the current work, where intermolecular interactions between radical and environment are at least minimally accounted for in the *g*-tensor calculation. The B3LYP level of theory was maintained for the entire cluster, but now only the atoms of the central radical were described using the 6-311G** basis set, along with those of two nearby water molecules. The other atoms of the cluster were still included in the calculation, but they were considered at the much smaller 3-21G basis set level (*26, 27*). The two water molecules were selected in the high basis set layer, because they are hydrogen bound to oxygen O_4 and effectively make up the immediate environment of the radical center. This mixed basis set scheme offers an affordable way to determine the *g* tensor without neglecting the crucial interactions between the central radical and the molecules in its close environment.

For reference, *g*-tensor properties were also calculated on geometries optimized within a ⟨a2bc⟩ supercell, adopting a consistent periodic approach as described in ref. (*28*). For these calculations, a BLYP functional form (*29, 30*) was used, together with a 100-Ry cutoff plane-wave basis set and Goedecker-type norm-conserving pseudopotentials (*31*). The parameters related to the evaluation of the *g*-tensor contributions in this approach included a threshold value of 0.05 for the magnetic response calculation and an ionic charge potential contribution to the effective potential close to the Coulomb limit [see ref. (*28*) for further information].

RESULTS AND DISCUSSION

Energetic Considerations of Proton Transfer

Following the suggestion in the measurements of Budzinski and Box that the dissociated hydroxyl proton was still in the vicinity of the radical center (O_4), proton transfer from this oxygen was considered. Such a mechanism assumes that the positive charge is (more or less) located on the H_{O4} hydroxyl proton after ionization and that it migrates into the molecular environment, generating the alkoxy species. This migration will follow the path of the original hydrogen bond, which, in the undamaged structure, extends between H_{O4} and the oxygen of a crystal water molecule.

The onset of this reaction is immediately after the ionization event. Hence the system has just been oxidized (an electron has been ejected), leaving the periodic ⟨2a2b2c⟩ supercell positively charged. Within the computational approach, this is compensated by a (nonlocalized) uniform negative charge background to prevent the unphysical sit-

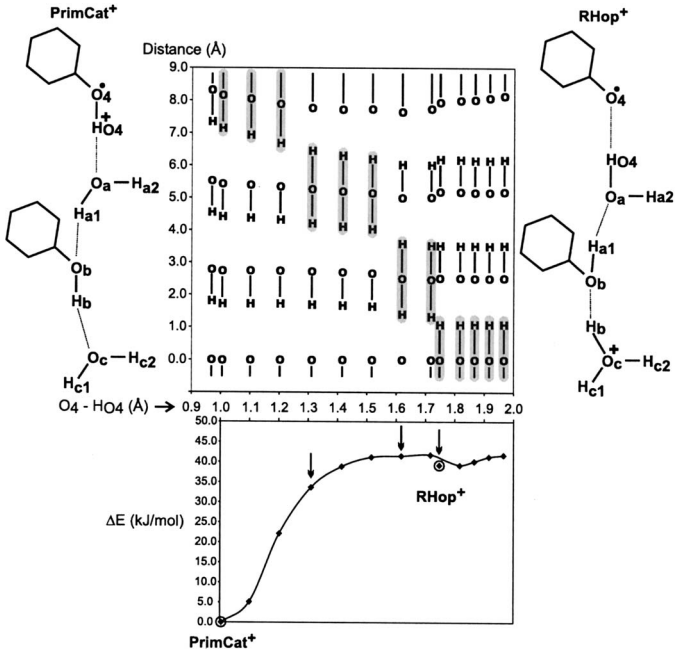

FIG. 2. Overview of energy and structural changes upon elongation of the O_4–H_{O4} bond. ΔE is considered relative to the **PrimCat**$^+$ binding energy (−2222.707 atomic units). Optimized points corresponding to the **PrimCat**$^+$ and **RHop**$^+$ structures are indicated by a circle. Arrows point out proton transfers. For O_4, H_{O4}, O_a, H_{a1}, O_b and H_b, absolute distances are plotted with respect to O_c. The gray highlighted regions indicate the main location of the positive charge.

uation in which the periodic system would get an infinite charge. Starting from the ideal crystal structure, the ionized supercell is optimized without geometric constraints. A symmetrical structure is obtained with the unpaired electron density distributed evenly over (mainly) C_4 and O_4 of all the molecules in the unit cell. The absolute binding energy for the entire cell containing this primary cation structure (labeled **PrimCat**$^+$) is −2222.707 atomic units. Subsequently, the H_{O4}–O_4 bond of one molecule is increased systematically and the system is reoptimized at each point under that constraint. This results in the energy profile presented in the lower half of Fig. 2. The energy difference (in kJ/mol) is considered relative to **PrimCat**$^+$, corresponding to an H_{O4}–O_4 bond distance of about 1.0 Å. The energy of the rhamnose system increases steadily with increasing bond distance until a shallow, local minimum is encountered around 1.85 Å. Along this path, three proton transfers throughout the periodic structure have taken place (at each time indicated by an arrow), although constraints were imposed on only one of the protons. This is illustrated in the top of Fig. 2, where the distances of all atoms involved with respect to O_c are plotted as a function of the constrained H_{O4}–O_4 distance. Gray highlighted regions indicate the main location of the positive charge.

The distances in the undamaged crystal are given for reference at an H_{O4}–O_4 bond length of 0.968 Å. This pattern is not altered much when the entire supercell is ionized. One could visualize the **PrimCat**$^+$ as represented at the left of the plot: Charge and spin density are both still located on the same rhamnose molecule. When the O_4–H_{O4} distance is increased to about 1.3 Å, a first proton transfer occurs. The spin density now becomes firmly localized on O_4, whereas the H_{O4} proton (and hence the charge) is transferred along the hydrogen bond to one of the crystal waters (labeled ''a''). As a result, the alkoxy radical is formed, connected to this $H_3O_a^+$ species with a hydrogen bond. However, this does not correspond to a minimum on the potential energy surface. Only when the O_4–H_{O4} distance is further elongated, thus increasing the distance between the water molecule and the alkoxy radical, is a second minimum eventually found. Between 1.5 and 1.85 Å, two further proton transfers occur. First, the H_{a1} proton of $H_3O_a^+$ is transferred to oxygen O_4 (labeled O_b in the plot) of a rhamnose molecule further away, briefly generating an $R–O_bH_2^+$ cation. Finally, the original H_{O4} proton of this rhamnose (labeled H_b) is in turn transferred to crystal water (O_c), again resulting in an $H_3O_c^+$ species. The stability of the final species resulting from the three proton transfers was verified by reoptimization without constraints (indicated by a circle). This structure, with absolute energy of −2222.692 atomic units, is depicted on the right side of Fig. 2 (referred to as **RHop**$^+$) and has an H_{O4}–O_4 distance of 1.748 Å. In contrast with the **PrimCat**$^+$, the charge is now separated from the main site of the unpaired spin density by almost 8 Å, incidentally comparable to half the length of the ⟨2a2b2c⟩ supercell along the crystallographic *b* axis.

The consecutive proton transfers bear a striking resemblance to the classical Grotthuss mechanism in solutions (*32–35*), where sequential proton ''hops'' between an initial donor and ultimate acceptor are mediated by water molecules or ionizable functional groups, extending along an extensive network. In the case of rhamnose, the three proton hops to go from **PrimCat**$^+$ to **RHop**$^+$ occur along a so-called infinite hydrogen bond chain or ribbon. As illustrated in Fig. 3, this chain extends throughout the crystal along the direction of the *b* axis, alternately connecting the O_4–H_{O4} hydroxyl groups of rhamnose molecules with crystal waters. Hence it is a suitable route for the proton to diffuse through the crystal matrix after ionization at a certain site. Similar proton transfers, or ''multi-proton shuffles'', have been proposed in crystals of nucleic acids, such as cytosine (*36*), adenosine (*37*) or cocrystals of methylcytosine and fluorouracil (*38*).

Attempts were made to initiate further proton jumps along the chain in rhamnose by systematically extending the H_{c1}–O_c bond in **RHop**$^+$. This resulted in a steep uphill potential, indicating that, within this model space, only a structure characterized by three proton jumps constitutes a (local) minimum along this relaxation route. However, the distance between the charged and the spin sites in **RHop**$^+$ (also shown in Fig. 3) is connected to the size of the simulation cell. The ⟨2a2b2c⟩ supercell is 2**b* wide (15.844 Å) in the direction of the *b* axis, implying that the charged site is (roughly) in the middle between the spin site (at a distance $+b$) and its periodic image (at a distance $-b$). This

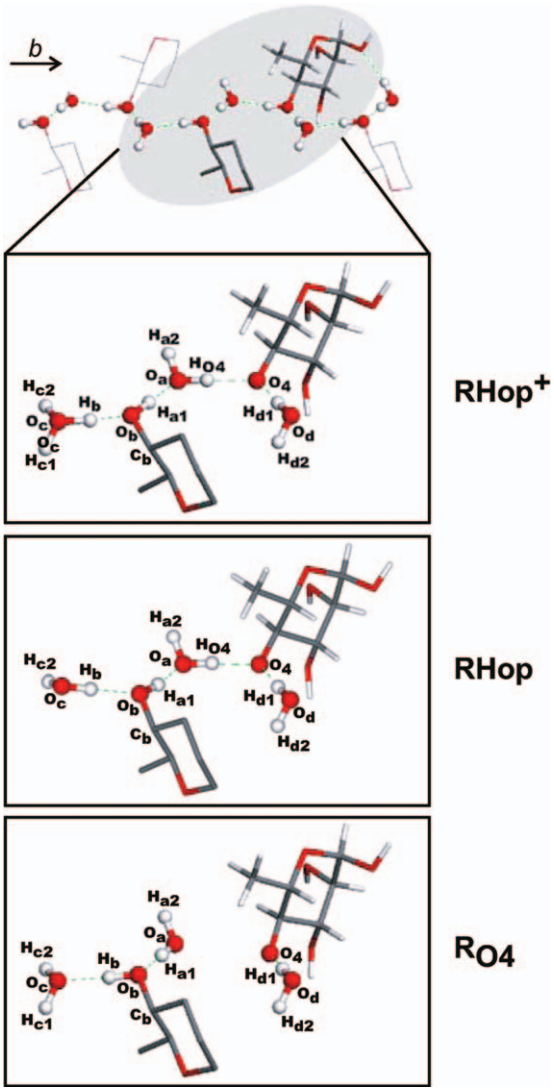

FIG. 3. View of the **RHop**$^+$, **RHop** and **RO4** species along the infinite hydrogen bond chain (*b* axis). A fragment of the intact crystal structure is shown at the top. All H and O atoms that are involved in the hydrogen bond chain are presented as balls.

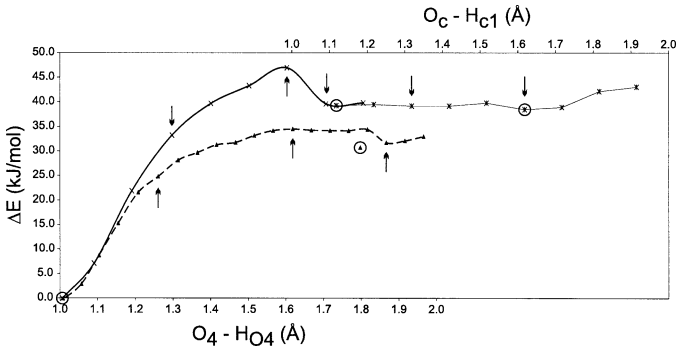

FIG. 4. Energy change upon elongation of the O_4–H_{O4} bond in the ⟨a2bc⟩ (▲) and ⟨a3bc⟩ (×) model space and upon further elongation of the O_c–H_{c1} bond in ⟨a3bc⟩ (*). The energy of the **PrimCat**$^+$ species is taken as reference (respectively −555.686 and −833.520 atomic units). Optimized points are indicated by circles, arrows point out proton transfers.

seems to suggest that the proton is ''trapped'' between the two spin sites in this model space and that additional proton hops would become possible if the supercell would be further enlarged along *b*.

Additional calculations on ⟨a2bc⟩ and ⟨a3bc⟩ supercells confirm this statement. In Fig. 4, the energy change upon H_{O4}–O_4 elongation in these supercells is plotted, resulting in energy profiles similar to that in Fig. 2. Here also, a minimum is encountered at 1.8 Å for ⟨a2bc⟩ and 1.75 Å for ⟨a3bc⟩, the latter perfectly comparable to the H_{O4}–O_4 distance for **RHop**$^+$ in the ⟨2a2b2c⟩ supercell. Three proton hops occur in the smallest model space (⟨a2bc⟩), yielding a 7.0 Å separation between the charged site (O_c) and the spin site (O_4). However, in the ⟨a3bc⟩ supercell, two further proton jumps along the infinite hydrogen bond chain are energetically favorable when additionally elongating the O_c–H_{c1} bond! Starting from a **PrimCat**$^+$ species, all together, five proton transfers take place in this model space before the charge is finally located on an H_3O^+ species, 10.6 Å away from the O_4 radical center. Since the ⟨a3bc⟩ supercell is 23.766 Å wide along *b*, the charged site is again nicely situated between the spin site (at +3/2 *b*) and its periodic image (at −3/2 *b*). Extrapolating these results, it is clear that the separation between the charge and the unpaired spin density is proportional to the length of the simulation cell along the *b* axis. In reality, of course, an irradiated crystal will not display the perfect supercell periodicity as in the simulations. The ionization sites will be distributed randomly throughout the matrix at relatively long distances from each other. For each such ionization site, the infinite hydrogen bond chain effectively represents something like a conductor channel, along which charge can migrate throughout the crystal matrix.

However, proton migration requires that the initial large energy barrier of about 40 kJ/mol has been crossed. This is not unlikely given that high-energy radiation is applied in these studies [γ rays in ref. (*9*), X rays in ref. (*10*)], often for several minutes. Also, tunneling or excited-state dynamics is likely to be involved in the proton transfer process. Furthermore, it is plausible that the migrating charge will become trapped at some point along the infinite hydrogen bond chain, for instance, when a radiation-induced anion is encountered further on in the crystal matrix. In a study of crystalline nucleic acids (*36*), it is even suggested that the mutual occurrence of both reduction and oxidation products is likely to be observed along this chain. Since the proton can readily move along the channel, it will transfer from the cation site to the anion site, hence irreversibly canceling out the charges and leaving behind two neutral radicals. In rhamnose, such neutralization would effectively prevent back-reaction and recombination with the alkoxy species, driving the system in the direction of **RHop**$^+$ formation. In fact, the mere occurrence (or observation) of a **PrimCat**$^+$ species seems highly unlikely, since it would require that oxidation of the rhamnose crystal would lead to a perfect

TABLE 2
Overview of Calculated *g* and Hyperfine Tensors for the RHop Alkoxy Species, Optimized in a ⟨2a2b2c⟩ Supercell Periodic Approach

	A_{iso}/g_{iso}	A_{aniso}/g_{aniso}	Direction cosines vs ⟨a*bc⟩			Ψ	A_{iso}/g_{iso}	A_{aniso}/g_{aniso}	
H2	61.6	−3.8	0.736	−0.481	−0.476	1	67.2	−4.0	BB−5
		−0.7	0.608	0.160	0.778	26		−0.2	
		4.5	0.297	0.862	−0.410	26		4.3	
H3	1.6	−10.0	−0.117	0.199	0.973	2	5.2	−12.7	BB−2
		−0.8	0.856	0.517	−0.003	7		−0.2	
		10.8	−0.504	0.833	−0.231	7		12.9	
H4	40.7	−5.7	0.219	0.716	0.663	2	53.9	−7.7	BB−6
		−3.9	−0.413	−0.548	0.728	3		−2.0	
		9.6	0.884	−0.433	0.175	3		9.7	
H6a	2.5	−1.9	0.711	−0.625	0.323	4	3.9	−1.9	BB−7
		−0.7	0.634	0.768	0.092	6		−0.7	
		2.5	−0.306	0.139	0.942	7		2.6	
HO3	−5.7	−7.7	−0.546	0.788	0.284	5	−5.2	−7.9	BB−4 (xc)
		−0.5	0.762	0.609	−0.223	5		0.1	
		8.2	0.348	−0.095	0.933	5		7.8	
HO4	−6.6	−11.4	0.608	0.010	0.794	30	−3.0	−7.7	BB−1 (xc)
		−10.3	0.778	0.187	−0.599	31		−7.3	
		21.8	−0.155	0.982	0.106	8		15.1	
Hd1	−0.1	−7.8	0.208	0.575	0.791	27	0.1	−5.9	BB−3 (xc)
		−6.2	0.349	0.712	−0.609	26		−4.9	
		14.0	0.914	−0.403	0.052	4		10.8	
g	2.0112	2.0030	−0.314	−0.704	0.637	2	2.0096	2.0018	BB−g
		2.0087	−0.569	0.676	0.468	1		2.0068	
		2.0220	−0.760	−0.215	−0.613	1		2.0202	
						35	2.0184	2.0032	SL−g
						34		2.0064	
						7		2.0456	

Note. Hyperfine couplings are in MHz, Ψ angle deviations with experiment in degrees.

distribution of the remaining unpaired electron over all molecules. However, multiple ionization and excitation events will be induced by radiation, giving rise to a disorganized and asymmetrical distribution of the spin density.

Of course, when the ejected proton has migrated along the hydrogen bond chain and has possibly recombined at some point with an anionic species, the positive charge is well separated from the alkoxy radical. The (local) geometry of the radical and its direct environment will no longer be influenced by the presence of a positive charge, nor will its EPR properties. To account for this possibility in the simulations, the ⟨2a2b2c⟩ rhamnose supercell was reoptimized after the removal of either the H_{c1} or H_{c2} protons from the **RHop**$^+$ species (see Fig. 3), effectively making the supercell neutral in the calculation. In both cases, this resulted in a significant displacement of the hydrogens and oxygens involved in the infinite hydrogen bond chain, though largely restricted to the locus of the removed proton. The geometry of the alkoxy radical was virtually unaltered. Removal of the H_{c1} proton (absolute energy −2222.004 atomic units) proved to be slightly favored over H_{c2} elimination (−2222.003 atomic units), which makes sense since the latter would disrupt the infinite hydrogen bond chain. With respect to **RHop**$^+$, the energy of the species obtained by removing H_{c1} (dubbed **RHop**) formally increases by more than 0.68 arbitrary units. However, this energy increase does not really constitute a barrier, under the assumption that the proton is not removed altogether from the system but rather migrates at a sufficiently long distance from the alkoxy species. The structure of the **RHop** species is also shown in Fig. 3.

EPR Properties of RHop

The calculated EPR spectroscopy properties of the **RHop** radical are presented in Table 2. Both the hyperfine and *g*-tensor data are separated into an isotropic (A_{iso} or g_{iso}) and an anisotropic part. Diagonalization of the latter matrix produces anisotropic couplings (or principal values A_{aniso}/g_{aniso}) and corresponding eigenvectors (or principal directions), expressed as direction cosines with respect to the orthogonal ⟨*a**bc*⟩ crystal axis reference frame. The Ψ angle (in degrees) reflects the deviation in orientation between the calculated eigenvectors and their experimental counterparts.

Overall, the close match with the Alk_{BB} measurements is remarkable. The calculations predict two main proton hyperfine couplings for this radical (61.6 and 40.7 MHz) that are significantly closer to the Alk_{BB} than to the Alk_{SL} results. What is more, the *g* tensor is in perfect agreement with the measurement of Budzinski and Box: *g*-tensor components agree closely, and the calculated eigenvectors deviate by less than 2° from the measured eigenvectors! The

assignment is further corroborated by several smaller hyperfine coupling tensors, many of which were detected in the EPR experiment. Since the isotropic coupling for these proton tensors is close to zero, their anisotropy is perhaps the most characteristic feature. Based on the correspondence between the calculated EPR properties for the **RHop** model and the Alk_{BB} data, several incorrect assignments were identified in the latter. In the following, this comparison is discussed briefly for each proton hyperfine tensor.

H_2. The calculated isotropic coupling for this proton is very close to the measured value of 67.2 MHz for the BB-5 signal. Interestingly, Budzinski and Box attributed this signal to a δ coupling: from one of the methyl protons on C_6. In the **RHop** model, the unpaired electron density on O_4 interacts with an equally distant proton on the other side of the pyranose sugar ring (H_2).

H_3. As Budzinski and Box mentioned with respect to their BB-2 signal, this tensor indeed ''has the characteristics of a strongly coupled γ proton.'' However, this signal does not correspond to H_5 as was suggested but rather to the other γ coupling, H_3. The agreement between the measured data and the calculations is very good for isotropic and anisotropic couplings as well as for the eigenvectors.

H_4. The calculated tensor for this proton is attributed to the BB-6 signal, despite the 13 MHz difference in isotropic coupling. However, as has been demonstrated on many occasions (*18, 39*), the isotropic coupling is rather sensitive to the level of theory. Thus the reported difference is not uncommon. The anisotropic couplings and eigenvectors, on the other hand, agree very well between theory and experiment.

H_{6a}. The BB-7 signal, originally attributed to the H_3 γ coupling, is found to be in excellent agreement with the calculated EPR hyperfine tensor of H_{6a}, one of the methyl group protons. The level of agreement for this remote δ proton is of rare quality, with almost perfectly reproduced isotropic and anisotropic couplings and Ψ deviations well below 10°.

H_{O3}. Among the Alk_{BB} hyperfine tensors, three of them were found to be exchangeable upon deuteration (BB-1, BB-3 and BB-4). The calculations corroborate the assignment of BB-4 to the H_{O3} hydroxyl proton. In Table 2, comparison is made with the measured tensor with negative isotropic hyperfine coupling, reversing the order of the anisotropic couplings. Absolute determination of the sign of a hyperfine constant is difficult from the experimental point of view, justifying the modification.

H_{O4}. Again, the calculated tensor for this proton affirms the experimental assignment to the dissociated H_{O4} proton, 1.681 Å from the $^{\bullet}O_4$ center in model **RHop**. Calculated hyperfine couplings are in excellent agreement with their experimental counterparts, but a Ψ correspondence lower than 10° is obtained only for the eigenvector with maximum principal component. This effect has been encountered in other studies (*19, 20*) and indicates the quasi-degeneracy for both minor anisotropic interactions, as conveyed by the mutual occurrence of virtually identical but rather large angles for these interactions.

H_{d1}. The last of the exchangeable couplings (BB-3) can be attributed to H_{d1}, which is one of the protons in the crystal water on the other side of the dissociated H_{O4}. The position and orientation of this water molecule are most easily seen in Fig. 3. Comparison between theory and experiment is similar to the case for H_{O4} and overall is very good.

Despite the few incorrect assignments, the accuracy and detail of the original Alk_{BB} EPR measurements are stunning. Furthermore, their accordance with the calculated spectroscopy data, which is both qualitative and quantitative in nature, leaves little doubt that the proposed **RHop** model is valid. Hence, in their 4.2 K measurement on irradiated rhamnose crystals, Budzinski and Box have effectively observed an alkoxy radical precursor obtained by proton transfer along an infinite hydrogen bond chain.

Energetic Considerations of Rearrangement

After consecutive proton hops, a Grotthuss mechanism would also involve a rearrangement of the water molecules to restore the hydrogen bonding network in its initial state. Hence it is sometimes referred to as a ''hop-and-turn'' process because the water molecules have to reorient. This field has been studied exhaustively [for a review, see ref. (*40*)], spurred by its importance in, for example, conducting proteins like gramicidin [e.g. ref. (*41*)]. In rhamnose single crystals, such a reorientation step can provide the link between the individual observations of apparently different types of alkoxy radicals at different temperatures.

In an earlier theoretical study (*12*), a structure was determined for the alkoxy radical as measured by Samskog and Lund. This **RO4** radical is obtained by removing the H_{O4} hydrogen from the model space. To allow comparison with the results in the current work, the geometry for this radical was reoptimized within a ⟨2a2b2c⟩ supercell approach. The resulting geometry (partially shown in Fig. 3) has an absolute energy of −2222.016 atomic units, which is some 30 kJ/mol lower than that of **RHop**! When the structure of the molecules in the vicinity of the **RHop** and **RO4** radicals is compared (shown in Fig. 3), it is apparent that the main difference lies in the orientation of hydroxyl groups and water molecules. Similar to the Grotthuss mechanism, three rearrangements would suffice to transform **RHop** into **RO4**:

1. rotation of H_b about the O_c–H_{c2} bond over 94° (clockwise),
2. rotation of H_{a1} about the O_b–C_b bond over 134° (counter clockwise), and
3. rotation of H_{O4} about the O_a–H_{a2} bond over 104° (counter clockwise).

In Fig. 5, the energy of the ⟨2a2b2c⟩ system (relative to that of **RHop**) is plotted as a function of these three rotation angles. The encircled points on the graph indicate fully optimized structures; all other points were obtained from constrained geometry optimizations. Apart from the constraint

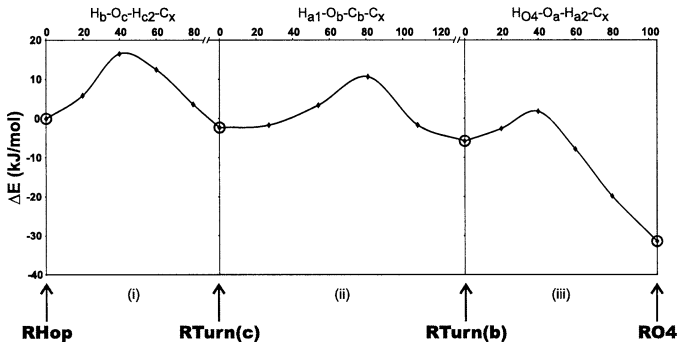

FIG. 5. Energy change upon sequential hydrogen bond rearrangement, relative to **RHop** (−2222.004 atomic units). All dihedral angles (in degrees) are referred to distant carbon atoms C_x further on in the crystal lattice. Circles indicate points that were obtained by full optimization (without constraints).

on the rotation angle, the Cartesian coordinates of the O_c and O_a oxygen atoms were also restrained in space for (1) and (3). The latter restrictions were imposed to prevent translation of the water molecules within the crystal matrix as much as possible. For clarity, only the change in the dihedral angles is reported, relative to its value in the optimized geometry from which the rotation was initiated.

The figure shows that two stable, local minima are encountered when consecutively rearranging the hydroxyl groups in the order (1)-(2)-(3). The structures **RTurn(c)** and **RTurn(b)** were obtained through unrestricted geometry optimizations and are slightly more stable than the **RHop** radical. When H_{O4} finally is rotated about the O_a–H_{a2} bond, the energy has dropped by 30 kJ/mol, indicating that **RO4** is significantly more stable than **RHop**. The energy barriers that have to be crossed are not exceedingly large, although they still amount to 10–15 kJ/mol. Even though this is inevitably a slight overestimation of the true barrier, because of the imposed constraints, the mere presence of these barriers is enough to prevent the transformation of **RHop** into **RO4** at temperatures as low as 4.2 K. Hence the rearrangement barriers allow the separate isolation and identification of an **RHop** species in the measurements of Budzinski and Box. At a temperature of 77 K, the system might just have acquired enough thermal energy to attain the more stable **RO4** species, as measured by Samskog and Lund. Thus it appears that in the radiation-induced alkoxy radical formation in rhamnose, hydrogen bond rearrangement is the slowest step. Comparable conclusions have been reached in computational studies of proton conduction in the ''water wire'' of the gramicidin protein (*42*). Although the hydroxyl group rearrangements were conducted consecutively in the order (1)-(2)-(3), it is doubtful that this exact sequence is followed in a real irradiated rhamnose crystal. First, many more than three proton hops will occur in rhamnose crystals, as argued above, which necessitates the rearrangement of multiple hydroxyl groups to attain the **RO4** species. Second, it is not clear whether these rearrangements occur consecutively or rather simultaneously.

EPR Properties of RO4

Using the ⟨2a2b2c⟩ supercell optimized **RO4** geometry, the EPR properties for this radical were calculated in accordance with the computational protocol adopted in the current work (Table 3a). To enable comparison with the EPR results for the **RHop** species, all proton tensors have been reported except for H_{O4}, which is not present in this system. It is immediately clear that the current results deviate to a larger extent from experiment than the results of previous calculations (as reported in Table 1). Most dramatically, the maximum anisotropic *g*-tensor component has dropped from an excellent 2.0456 to 2.0263. Based solely on this parameter, the **RO4** radical would be in better agreement with the measurement of Budzinski and Box than with that of Samskog and Lund. However, the H_2 and H_4 isotropic hyperfine couplings are still in significantly better agreement with the latter experimental data, even though the quantitative accordance is somewhat less. These discrepancies between current and previous calculations have two origins:

1. The geometries for which the EPR properties were calculated are not identical, because they were obtained with different methodologies. In ref. (*12*), a cluster approach was adopted under the constraint that the molecular environment of the radical remained identical to the crystal structure. In the current work, none of these constraints apply.
2. As mentioned in above, the *g* tensor in the previous work was calculated on the basis of a single molecule approach, i.e., without any of the neighboring molecules present in the model space (not even the water molecules). This is in sharp contrast to the current computational protocol, in which the environment is taken into account for the *g*-tensor calculation.

To quantify the effect of the latter, the current computational procedure for *g*-tensor calculation was applied on the cluster-optimized geometry from the previous work (Table 3b). Compared to the original calculated data for **RO4** in Table 1, the maximum anisotropic *g*-tensor component is already significantly smaller (2.0303)! As regards the first factor, the **RO4** cluster geometry from the previous work and the present geometry are very similar, with a root mean square deviation of only 0.19 Å. Yet even such slight conformational changes seem to have a significant impact on the *g* tensor, as is exemplified in Table 3b. The maximum anisotropy changes from 2.0263 to 2.0303, which is indisputably related to the small difference in both geometries since the same computational protocol was used for both calculations.

To further distinguish the *g* tensors between **RHop** and **RO4**, additional calculations were performed using a periodic formalism as described in ref. (*28*). Since the

TABLE 3
Calculated *g* and Hyperfine Tensors for the RO4 Alkoxy Species Calculated on the Radical Geometry as Optimized in a ⟨2a2b2c⟩ Supercell Periodic Approach and on the Radical Geometry as Obtained from Previous Work (*12*)

	A_{iso}/g_{iso}	A_{aniso}/g_{aniso}	Direction cosines vs ⟨a*bc⟩			Ψ	A_{iso}/g_{iso}	A_{aniso}/g_{aniso}	
a. on radical geometry from ⟨2a2b2c⟩ periodic optimization									
H2	50.4	−3.5	0.692	−0.528	−0.492		39.2		SL−2
		−0.3	0.579	−0.001	0.815				
		3.8	0.431	0.849	−0.305				
H3	−1.7	−10.3	−0.160	0.150	0.976				
		−0.3	0.943	0.316	0.106				
		10.6	−0.293	0.937	−0.192				
H4	87.1	−5.9	0.443	0.881	0.163		112.1		SL−1
		−4.6	−0.209	−0.075	0.975				
		10.5	0.872	−0.466	0.151				
H6a	1.1	−1.5	0.705	−0.672	0.226				
		−0.8	0.654	0.740	0.156				
		2.4	−0.272	0.038	0.961				
HO3	−4.0	−6.6	−0.460	0.865	0.202				
		0.9	0.881	0.474	−0.024				
		5.7	0.116	−0.167	0.979				
Hdl	−0.3	−11.1	0.175	0.385	0.906				
		−8.0	0.278	0.864	−0.420				
		19.1	0.944	−0.325	−0.045				
g	2.0125	2.0023	−0.316	−0.839	0.443	14	2.0096	2.0018	BB−g
		2.0087	−0.547	0.542	0.637	13		2.0068	
		2.0263	−0.775	−0.041	−0.631	9		2.0202	
						24	2.0184	2.0032	SL−g
						25		2.0064	
						6		2.0456	
b. on radical geometry from cluster optimization									
g cluster	2.0138	2.0023	−0.294	−0.870	0.396	17	2.0096	2.0018	BB−g
		2.0087	−0.626	0.488	0.608	15		2.0068	
		2.0303	−0.722	−0.069	−0.688	9		2.0202	
						21	2.0184	2.0032	SL−g
						21		2.0064	
						3		2.0456	

Note. Hyperfine couplings are in MHz, Ψ angle deviations with experiment in degrees.

⟨2a2b2c⟩ supercell approach proved too demanding computationally for this scheme, analogous **RHop** and **RO4** optimized geometries were taken from the ⟨a2bc⟩ supercell calculations. The results are presented in Table 4. Concentrating on the variation in the maximum anisotropic *g*-tensor component, the periodic approach yields results that are consistent with the mixed basis approach of Tables 2 and 3. Both computational approaches rigorously take into account the molecular environment of the radical and succeed in qualitatively reproducing the dissimilarity between the experimental Alk_{SL} and Alk_{BB} *g* tensors. The origin of the residual difference with respect to experiment is unclear and calls for further investigation.

Comparison of the RHop and RO4 Alkoxy Radicals

Probably the most striking feature in both the **RHop** and **RO4** variations of the rhamnose alkoxy radical is the occurrence of the large H_2 δ couplings. Although this proton is located about 4.56 Å, respectively 4.49 Å from the radical center, the unpaired electron density at this site is still sufficiently large to result in couplings of 61.6 or 50.4 Mhz. δ couplings of this magnitude are quite rare, and their occurrence in rhamnose can be understood by considering the unpaired spin density plots in Fig. 6a. Contrary to what would be expected *a priori*, the unpaired electron density is not just simply localized on oxygen O_4, but rather it is notably delocalized over several nuclei in the radical. The plots further exemplify that considerable spin density is present in between C_4 and C_3 in both **RHop** and **RO4**. This is indicative of resonance states that contribute to the calculated density, as illustrated in Fig. 6b. The resonance structure on the left represents the classical view of the alkoxy radical, with the unpaired electron localized mainly on oxygen O_4. In the second resonance conformer, the spin density is concentrated on C_3, O_4 is involved in a double bond with C_4, and the C_3–C_4 bond has been broken. The contribution of this resonance structure is attested by a reduced O_4–C_4 bond length (1.34 Å in both **RHop** and **RO4** compared to 1.42 Å in undamaged rhamnose) and an increased C_3–C_4 bond length (1.67/1.65 Å in **RHop/RO4**

TABLE 4
Results of *g*-Tensor Calculations Adopting a Consistent Periodic Approach as Described in Ref. (*28*)

	g_{iso}	g_{aniso}	Direction cosines vs ⟨a*bc⟩			Ψ(BB)	Ψ(SL)
RHop	2.0128	2.0048	−0.196	−0.810	0.553	12	25
		2.0110	−0.623	0.538	0.568	12	24
		2.0226	−0.758	−0.233	−0.610	2	8
RO4	2.0128	2.0027	−0.269	−0.915	0.302	24	16
		2.0106	−0.569	0.404	0.716	22	16
		2.0252	−0.777	0.021	−0.629	13	9

Note. Calculations were performed on **RHop** and **RO4** geometries optimized within an ⟨a2bc⟩ supercell.

compared to 1.52 Å in undamaged rhamnose). In the second resonance state, H_2 is no longer in a δ position with respect to the unpaired electron but instead has become a β coupling, which accounts for the size of its hyperfine splitting. A similar resonance mechanism was already suggested by Budzinski and Box, albeit not in rhamnose (*43*).

The differences between **RHop** and **RO4** can be understood in terms of this resonance. Due to the extra hydrogen bond in the former radical between O_4 and crystal water H_2O_a, the delocalization mechanism is extended to include this water, indicated by a non-zero spin density on it (Fig. 6a). Conversely, the larger *g*-tensor anisotropy in radical **RO4** is due to reduced delocalization (spin concentration) since it no longer disposes of this hydrogen bond with the crystal water. Since both variations of the alkoxy radical have similar structures, it is clear that they differ mainly in electronic configuration. Hence it is the molecular environment that discriminates the two variants and causes the marked differences in *g* and hyperfine tensors.

CONCLUSIONS

A Grotthuss-like mechanism is shown to be active in the radiation-induced formation of rhamnose alkoxy radicals. Starting from an adiabatically oxidized crystal structure, hydroxyl proton H_{O4} is transferred along an infinite hydrogen bond chain in the crystallographic ⟨b⟩ direction, likely toward a reduction site further on where the proton recombines. The resulting **RHop** radical species can then transform in a more stable radical form, dubbed **RO4**, through a number of (slow) water and hydroxy-group reorientations. Although only low barriers (∼15 kJ/mol) separate the two structures, it is put forward that they are sufficient for the former species to be isolated and observed at very low temperatures. Calculation of EPR properties and comparison with experimental data in the literature shows that the **RHop** radical is in very good agreement with the species observed by Budzinski and Box in EPR experiments at 4.2 K. Similar measurements at 77 K by Samskog and Lund reveal spectroscopic properties that are consistent with the calculated EPR parameters of the **RO4** species.

Hence calculations of the energetics associated with the mechanism as well as simulated spectroscopic properties support the assumption that different variants of the rhamnose alkoxy radical can be observed depending on the temperature of irradiation and consecutive EPR measurement. Both species differ only in their local molecular environment, where **RHop** is involved in an extra hydrogen bond interaction with crystal water compared to the more stable **RO4**. Due to the absence of this additional interaction, the spin density is more concentrated in the latter species, giving rise to typical variations in EPR properties, such as the maximum anisotropic *g*-tensor component (2.0456 compared to 2.0202) or the isotropic hyperfine couplings. The existence of rather large δ-type hyperfine couplings in both species was traced back to resonance contribution of a radical structure in which the pyranose sugar ring was broken. As a result, the unpaired spin density is delocalized over a large part of the rhamnose radical.

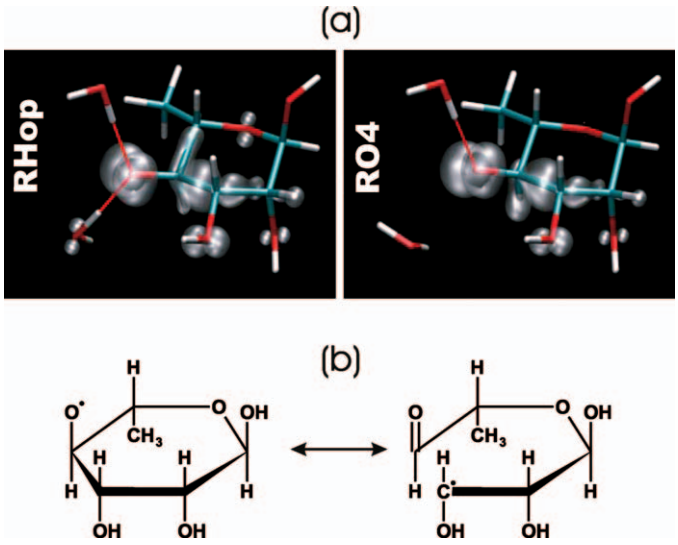

FIG. 6. Panel a: Unpaired spin density in the **RHop** and **RO4** radical species (at an iso value of 0.005). Panel b: Resonance structures contributing to spin density in C_3–C_4 bond give rise to large δ couplings.

ACKNOWLEDGMENTS

This work is supported by the Fund for Scientific Research – Flanders (FWO) and the Research Board of the Ghent University.

Received: March 22, 2007; accepted: September 4, 2007

REFERENCES

1. D. M. Close, Where are the sugar radicals in irradiated DNA? *Radiat. Res.* **147**, 663–673 (1997).

2. L. I. Shukla, R. Pazdro, D. Becker and M. D. Sevilla, Sugar radicals in DNA: Isolation of neutral radicals in gamma-irradiated DNA by hole and electron scavenging. *Radiat. Res.* **163**, 591–602 (2005).
3. A. Adhikary, A. Y. S. Malkhasian, S. Collins, J. Koppen, D. Becker and M. D. Sevilla, UVA-visible photo-excitation of guanine radical cations produces sugar radicals in DNA and model structures. *Nucleic Acids Res.* **33**, 5553–5564 (2005).
4. A. Adhikary, D. Becker, S. Collins, J. Koppen and M. D. Sevilla, C5′- and C3′-sugar radicals produced via photo-excitation of one-electron oxidized adenine in 2′-deoxyadenonsine and its derivatives. *Nucleic Acids Res.* **34**, 1501–1511 (2006).
5. E. E. Budzinski, W. R. Potter and H. C. Box, Radiation effects in X-irradiated hydroxy compounds. *J. Chem. Phys.* **72**, 972–975 (1980).
6. H. C. Box, E. E. Budzinski and H. G. Freund, Studies of electrons trapped in X-irradiated rhamnose crystals. *Radiat. Res.* **121**, 262–266 (1990).
7. P. O. Samskog, A. Lund, G. Nilsson and M. C. R. Symons, Primary reactions of localized electrons in rhamnose crystals studied by pulse-radiolysis and ESR spectroscopy. *J. Chem. Phys.* **73**, 4862–4866 (1980).
8. P. O. Samskog, L. D. Kispert and A. Lund, Geometric model of trapped electrons in X-ray-irradiated single-crystals of rhamnose. *J. Chem. Phys.* **79**, 635–638 (1983).
9. P. O. Samskog and A. Lund, The alkoxy radical RCHO formed in irradiated single crystals of rhamnose. *Chem. Phys. Lett.* **75**, 525–527 (1980).
10. E. E. Budzinski and H. C. Box, Alkoxy radicals—delta-proton hyperfine couplings. *J. Chem. Phys.* **82**, 3487–3490 (1985).
11. E. Sagstuen, M. Lindgren and A. Lund, Electron trapping and reactions in rhamnose by ESR and ENDOR. *Radiat. Res.* **128**, 235–242 (1991).
12. E. Pauwels, V. Van Speybroeck and M. Waroquier, Study of rhamnose radicals in the solid state adopting a density functional theory cluster approach. *J. Phys. Chem. A* **110**, 6504–6513 (2006).
13. S. Takagi and G. A. Jeffrey, Neutron-diffraction refinement of crystal structure of alpha-l-rhamnose monohydrate. *Acta Cryst. B* **34**, 2551–2555 (1978).
14. CPMD V3.11. ©IBM Corp. 1996–2006, ©MPI für Festkörperforschung Stuttgart 1997–2001.
15. J. P. Perdew, Density-functional approximation for the correlation energy of the inhomogeneous electron gas. *Phys. Rev. B* **33**, 8822–8824 (1986).
16. A. D. Becke, Density-functional thermochemistry 1: the effect of the exchange-only gradient correction. *J. Chem. Phys.* **96**, 2155–2160 (1992).
17. D. Vanderbilt, Soft self-consistent pseudopotentials in a generalized eigenvalue formalism. *Phys. Rev. B* **41**, 7892–7895 (1990).
18. M. Kaupp, M. Bühl and V. G. Malkin, *Calculation of NMR and EPR Parameters: Theory and Applications.* Wiley-VCH, Weinheim, 2004.
19. R. Declerck, E. Pauwels, V. Van Speybroeck and M. Waroquier, First-principles calculations of hyperfine parameters with the Gaussian and augmented-plane-wave method: Application to radicals embedded in a crystalline environment. *Phys. Rev. B* **74**, 245103 (2006).
20. E. Pauwels, V. Van Speybroeck and M. Waroquier, Evaluation of different model space approaches based on DFT to examine the EPR parameters of a radiation-induced radical in solid-state alpha glycine. *J. Phys. Chem. A* **108**, 11321–11332 (2004).
21. E. Pauwels, V. Van Speybroeck and M. Waroquier, Radiation-induced radicals in alpha-D-glucose: Comparing DFT cluster calculations with magnetic resonance experiments. *Spectrochim. Acta A* **63**, 795–801 (2006).
22. M. J. Frisch, G. W. Trucks, H. B. Schlegel, G. E. Scuseria, M. A. Robb, J. R. Cheeseman, J. A. Montgomery, Jr., T. Vreven, K. N. Kudin and J. A. Pople, Gaussian 03, Revision B.03. Gaussian, Inc., Wallingford, CT, 2004.
23. A. D. Becke, Density-functional thermochemistry 4: a new dynamical correlation functional and implications for exact-exchange mixing. *J. Chem. Phys.* **104**, 1040–1046 (1996).
24. R. Krishnan, J. S. Binkley, R. Seeger and J. A. Pople, Self-consistent molecular-orbital methods 20: basis set for correlated wave-functions. *J. Chem. Phys.* **72**, 650–654 (1980).
25. A. D. McLean and G. S. Chandler, Contracted Gaussian-basis sets for molecular calculations 1: 2nd row atoms, z = 11–18. *J. Chem. Phys.* **72**, 5639–5648 (1980).
26. J. S. Binkley, J. A. Pople and W. J. Hehre, Self-consistent molecular-orbital methods 21: small split-valence basis sets for 1st-row elements. *J. Am. Chem. Soc.* **102**, 939–947 (1980).
27. M. S. Gordon, J. S. Binkley, J. A. Pople, W. J. Pietro and W. J. Hehre, Self-consistent molecular-orbital methods 22: small split-valence basis sets for 2nd-row elements *J. Am. Chem. Soc.* **104**, 2797–2803 (1982).
28. R. Declerck, V. Van Speybroeck and M. Waroquier, First-principles calculation of the EPR *g* tensor in extended periodic systems. *Phys. Rev. B* **73**, 115113 (2006).
29. A. D. Becke, Density-functional exchange-energy approximation with correct asymptotic behavior. *Phys. Rev. A* **38**, 3098–3100 (1988).
30. C. T. Lee, W. T. Yang and R. G. Parr, Development of the Colle-Salvetti correlation-energy formula into a functional of the electron density. *Phys. Rev. B* **37**, 785–789 (1988).
31. S. Goedecker, M. Teter and J. Hutter, Separable dual-space Gaussian pseudopotentials. *Phys. Rev. B* **54**, 1703–1710 (1996).
32. C. J. T. de Grotthuss, Mémoire sur la décomposition de l'eau et des corps qu'elle tient en dissolution à l'aide de l'électricité galvanique. *Ann. Chim.* **58**, 54–74 (1806).
33. C. J. T. de Grotthuss, Memoir on the decomposition of water and of the bodies that it holds in solution by means of galvanic electricity. *Biochim. Biophys. Acta* **1757**, 871–875 (2006). [English translation by R. Pomès]
34. N. Agmon, The Grotthuss mechanism. *Chem. Phys. Lett.* **244**, 456–462 (1995).
35. P. Adelröth, Special issue on proton transfer in biological systems—Preface. *Biochim. Biophys. Acta* **1757**, 867–870 (2006).
36. W. A. Bernhard, J. Barnes, K. R. Mercer and N. Mroczka, The influence of packing on free radical yields in crystalline nucleic acids—the pyrimidine bases. *Radiat. Res.* **140**, 199–214 (1994).
37. W. H. Nelson, E. Sagstuen, E. O. Hole and D. M. Close, Electron spin resonance and electron nuclear double resonance study of X-irradiated deoxyadenosine: Proton transfer behavior of primary ionic radicals. *Radiat. Res.* **149**, 75–86 (1998).
38. D. M. Close, L. A. Eriksson, E. O. Hole, E. Sagstuen and W. H. Nelson, Experimental and theoretical investigation of the mechanism of radiation-induced radical formation in hydrogen-bonded cocrystals of 1-methylcytosine and 5-fluorouracil. *J. Phys. Chem. B* **104**, 9343–9350 (2000).
39. V. Barone, Structure, magnetic properties and reactivities of open-shell species from density functional and self-consistent hybrid methods. In *Recent Advances in Density Functional Methods, Part I* (D. P. Chong, Ed.), pp. 287–334. World Scientific, Singapore, 1995.
40. S. Cukierman, Et tu, Grotthuss! and other unfinished stories. *Biochim. Biophys. Acta* **1757**, 876–885 (2006).
41. R. Pomès and B. Roux, Molecular mechanism of H^+ conduction in the single-file water chain of the gramicidin channel. *Biophys. J.* **82**, 2304–2316 (2002).
42. R. Pomès and B. Roux, Free energy profiles for H^+ conduction along hydrogen-bonded chains of water molecules. *Biophys. J.* **75**, 33–40 (1998).
43. H. C. Box and E. E. Budzinski, A variation of the alkoxy radical. *J. Chem. Phys.* **79**, 4142–4145 (1983).